Journal of
Marine Science and Engineering

MDPI

Article

Numerical Simulation of Wave Interaction with Payloads of Different Postures using OpenFOAM

Mingwei Yan [1], Xin Ma [1,*], Wei Bai [2], Zaibin Lin [2] and Yibin Li [1]

[1] Center for robotics, School of Control Science and Engineering, Shandong University, Jinan 250061, China; yanmingwei1122@mail.sdu.edu.cn (M.Y.); liyb@sdu.edu.cn (Y.L.)

[2] Department of Computing and Mathematics, Manchester Metropolitan University, Chester Street, Manchester M1 5GD, United Kingdom; w.bai@mmu.ac.uk (W.B.); z.lin@mmu.ac.uk (Z.L.)

* Correspondence: maxin@sdu.edu.cn

Received: 10 May 2020; Accepted: 5 June 2020; Published: date

Abstract: A three-dimensional numerical wave tank (NWT) is established with Open Source Field Operation and Manipulation (OpenFOAM) software and waves2foam to investigate wave interaction with payloads with different postures in the process of offshore lifting or lowering. Numerical results of regular wave interaction with a vertically suspending cylinder are presented first for validation by comparison with the published data. A series of simulation experiments are carried out, and the forces and the moments exerted by the regular waves on a fixed suspending cylinder payload and a fixed suspending cuboid payload with different postures are presented. It can be concluded from the results that the rotating rectangular payload (cuboid and cylinder) suffers a drastically changed moment when it is initially vertically placed, and the projection area of payload vertical to the force affects the corresponding force. The simulation results also show how the forces and the moments change with different posture angles. With some certain posture, the suspending payload suffers minimum forces and moments. Parametric study for the cuboid payload is done in the case of normal incidence. The influence of the payload's size and wave parameters on forces and moments are analyzed. All of the numerical simulation results and conclusions provide the fundamentals for further research and safe control of offshore lifting or lowering.

Keywords: offshore crane; OpenFOAM; wave–payload interaction; NWT

1. Introduction

With ever-increasing marine exploration and subsea resource exploitation, offshore cranes which are mounted on vessels and carry out lifting/lowering have been widely used in marine operations. While working on the sea, offshore cranes suffer from persistent disturbances induced by ocean waves. During lifting or lowering, the payloads may be subject to large hydrodynamic forces, which could cause payload damages or cable breaks. This would further cause accidents and impair the safety of life and property [1].

In order to lift/lower payloads on the sea safely and efficiently, the capability to estimate the hydrodynamic loads on payloads is of vital importance. The hydrodynamic loads on stationary structures in waves have been studied for the safe and cost-effective design of coastal and offshore structures in the past decades. Compared to physical experiments, which need to establish scaled models, numerical modeling is more practical. The numerical models based on potential flow theory and Navier-Stokes (N-S) equations are two main categories for the simulation of wave-structure interactions.

The potential flow model is applied for wave interaction with large structures where viscous and turbulence effects can be ignored, such as the second-order potential flow theory model [2,3] and the fully nonlinear potential flow theory model [4]. With the assumption that the flow is inviscid and flow irrotational, it is challenging for the potential flow theory to capture the nonlinear free surface correctly when wave breaking occurs. Computational Fluid Dynamics (CFD) based on Navier–Stokes (N–S) equations is used for highly nonlinear wave–structure interactions in the case of breaking wave impacts and evolution of vortices. Various methods or models have been considered for wave–structure interaction, such as the Institute of Environmental Hydraulics of Cantabria Field Operation and Manipulation (IHFOAM) model, which solves Volume-Averaged Reynolds-Averaged Navier–Stokes equations (VARANS) [5,6], the multiple-layer σ-coordinate model [7], the Immersed Boundary Method [8], the Smooth Particle Hydrodynamics method [9,10], and the Constrained Interpolation Profile method [11].

OpenFOAM, a free open-source C++ toolbox for the development of customized numerical solver (such as the naoe-FOAM-SJTU solver [12]) based on CFD, has been applied in coastal and offshore engineering recently. Regular wave interaction with two tandem cylinders is studied with OpenFOAM [13], and an improved model named IHFOAM is used to study wave interaction with porous coastal structures [14,15]. The performance of OpenFOAM for nonlinear wave interactions with offshore structures is assessed, with up to eighth order harmonics correctly modeled [16].

In addition to the normal incident wave interaction with structures, many researchers have also investigated the interaction of oblique waves with stationary structures, such as perforated caissons [17], bridge decks [18], and various other structures [19–24]. The stationary nature of the structure makes it hard to rotate around different axes, the above oblique papers only focus on the situation of one single posture angle. Compared with stationary structures, the payloads can move with much more freedom while lifting or lowering payloads on the sea. Here, we want to reach a general conclusion when considering different posture angles, and to the authors' knowledge, there has been no previous research about the general postures' study of the payload.

Importantly, the posture of the payload has an impact on the force and moment exerted by the wave; additionally, the force and moment can also change the posture. This paper focuses on studying the influence of different postures of the payloads on wave forces and moments exerted on the payloads; thus, we assume that the payload is fixed without linear motion and rotation. A cylinder payload and a cuboid payload, both fixed and suspended with different postures in regular waves, are investigated, respectively. By carrying out a series of simulations, the influence of the payloads' posture angles relative to the regular waves on the hydrodynamic forces and moments exerted on the payloads are analyzed. It can be concluded from the results that the rotating rectangular payload (cuboid or cylinder) suffers a drastically changed moment when it is initially vertically placed, and the direction of the moment is the same as axis' rotation except for one situation. The projection area of the payload vertical to the force affects the corresponding force. The analysis could provide help for developing control strategies for offshore cranes, such as choosing the appropriate payload posture during water entry, and then using a controller to keep the payload on a certain posture that suffers minimal forces or moments during water entry.

2. Numerical Methods

2.1. Governing Equations

In order to represent the payload's posture in the wave, two Cartesian frames are defined, as shown in Figure 1a. The world frame $\left(o_w\text{-}\mathbf{x}_w\mathbf{y}_w\mathbf{z}_w\right)$ defined based on the 3D NWT. o_w is the midpoint of the inlet. $o_w\mathbf{x}_w$ is the direction of wave propagation. $o_w\mathbf{z}_w$ points straight upwards. The body frame is fixed with the payload. As for the body frame $\left(o_b\text{-}\mathbf{x}_b\mathbf{y}_b\mathbf{z}_b\right)$ of the cuboid payload, o_b is the centroid of the payload, and the three axes follow the directions of the three edges of the cuboid, respectively. The cuboid payload's posture in the wave can be expressed by the three Euler angles

θ, ϕ, ψ (pitch, roll, and yaw angles), which represent the pose relationship between the payload's body frame $(o_b\text{-}\mathbf{x}_b\mathbf{y}_b\mathbf{z}_b)$ and the world frame $(o_w\text{-}\mathbf{x}_w\mathbf{y}_w\mathbf{z}_w)$ as shown in Figure 1b.

Both air and water are assumed to be incompressible laminar fluid. The motion of the fluid continuum is described with the governing equations, i.e., the Navier–Stokes equations and the continuity equation [16],

$$\frac{\partial \rho}{\partial t} + \nabla \cdot (\rho \mathbf{U}) = 0 \tag{1}$$

$$\frac{\partial \rho \mathbf{U}}{\partial t} + \nabla \times (\rho \mathbf{U}\mathbf{U}) - \nabla \times (\mu \nabla \mathbf{U}) - \rho g = -\nabla p - f_\sigma \tag{2}$$

where $\mathbf{U}$ is the fluid velocity, ρ is the fluid density, p is the fluid pressure, μ is the dynamic viscosity, t is the time, g is the gravity acceleration, and f_σ is the surface tension. Only the laminar flow is considered in the study.

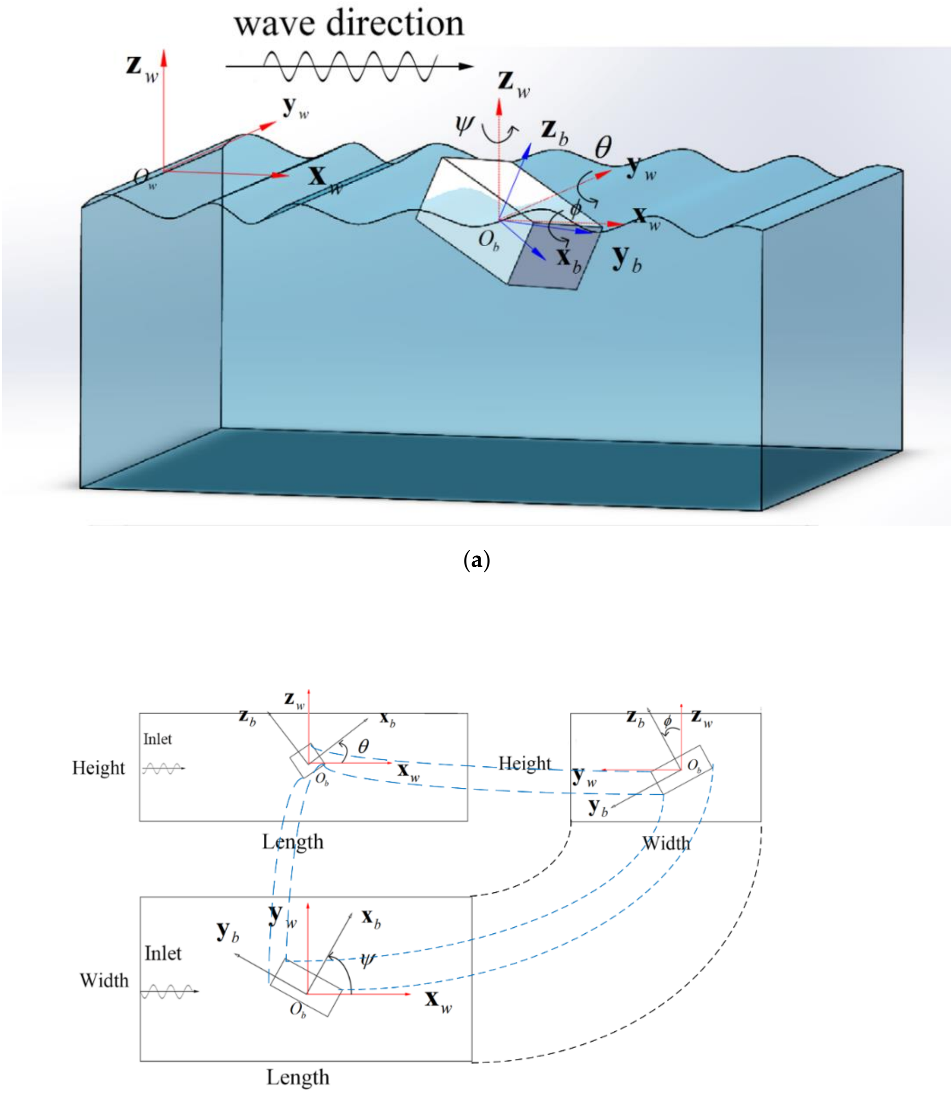

(**a**)

(**b**)

Figure 1. Two different descriptions of frames and the postures of the cuboid payload in the 3D numerical wave tank (NWT). (**a**) The overall description of two frames and a cuboid payload in the 3D NWT; (**b**) description of Euler angles in the top, side, and front view.

2.2. Free Surface Tracking

The Volume of Fluid (VOF) method is applied for tracking the free surface in OpenFOAM. In the VOF method, a phase function α is defined in each cell, which indicates the quantity of water in the cell. α is 1 if the cell is full of water, and it is 0 in empty cells. On the air-water interface, the value of α is between 0 and 1. The fluid density ρ and the dynamic viscosity μ in each cell are calculated with the equations,

$$\begin{aligned} \rho &= \alpha\rho_1 + (1-\alpha)\rho_2 \\ \mu &= \alpha\mu_1 + (1-\alpha)\mu_2 \end{aligned} \tag{3}$$

where the subscripts 1 and 2 mean the values of water and air, respectively. The phase function α can be determined by solving an advection equation,

$$\frac{\partial\alpha}{\partial t} + \nabla\cdot(\alpha\mathbf{U}) + \nabla\cdot(\alpha(1-\alpha)\mathbf{U}_\alpha) = 0 \tag{4}$$

where the last term on the left-hand side is an artificial compression term and $\mathbf{U}_\alpha$ is the relative compression velocity [25].

2.3. Waves2Foam Library and WaveFoam Solver

The library waves2Foam is used to generate regular waves. The boundary condition and solve procedures are listed below.

2.3.1. Waves2Foam Library

The library waves2Foam is a toolbox for generating and absorbing water waves [26]. Waves are generated at the inlet and absorbed at the outlet.

The velocities of regular waves are based on the linear Stokes' wave theory,

$$u(x,z,t) = \frac{gkA}{\omega}\frac{\cosh k(z+h)}{\cosh kh}\sin\varphi \tag{5}$$

$$w(x,z,t) = \frac{gkA}{\omega}\frac{\sinh k(z+h)}{\cos kh}\cos\varphi \tag{6}$$

where $u(x,z,t)$ is the horizontal velocity distribution, A is the wave amplitude, ω is the wave frequency, $\varphi = kx - \omega t$ and k is the wave number, h and is the water depth.

The relaxation zone technique is used to absorb waves at the outlet. The relaxation function is

$$\alpha_R(\chi_R) = 1 - \frac{\exp(\chi_R{}^{3.5}) - 1}{\exp(1) - 1} \quad \text{for } \chi_R \in [0:1] \tag{7}$$

It is applied into the relaxation zone as follows,

$$\lambda = \alpha_R\lambda_{\text{computed}} + (1-\alpha_R)\lambda_{\text{target}} \tag{8}$$

where λ is either $\mathbf{U}$ or α. The variation of α_R is the same as given in [27], and χ_R represents a certain point in the relaxation zone. The definition of χ_R is such that it is always 1 at the interface between the nonrelaxed part of the computational domain and the relaxation zone.

2.3.2. WaveFoam Solver and Boundary Conditions

1. Boundary conditions

The boundary name is just as shown in Figure 2. At the inlet of the 3D NWT, a specified boundary condition of fluid velocity $\mathbf{U}$ is set to *waveVelocity*, the boundary condition of the indicator phase function α is set to *waveAlpha*, and the boundary condition of the fluid pressure p is set to *zeroGradient*. At the top of the NWT, the velocity $\mathbf{U}$ is set to *pressureInletOutletVelocity*, which is a default boundary condition in OpenFOAM, the pressure p is set to *totalPressure*, and the phase function α is set to *inletOutlet*.

For the remaining parts of the NWT and the fixed suspending objects, the boundary conditions are considered as solid walls, where the fluid velocity $\mathbf{U}$ is set to a fixed value of zero, the fluid pressure p and the indicator phase function α are set to *zeroGradient.*

2. Solving procedure

The *waveFoam* solver starts with the preprocessor, which is used to set up wave properties and computational meshes. The meshes of the NWT are generated by using the built-in tool *blockMesh* and *snappyHexMesh*. The N–S equations are discretized into a set of algebraic equations by integrating the boundary conditions over the whole solution domain and time domain. The physical parameters of the whole domain like the fluid pressure p and the fluid velocity $\mathbf{U}$, etc., are calculated and updated at each timestep by calling solver *waveFoam*.

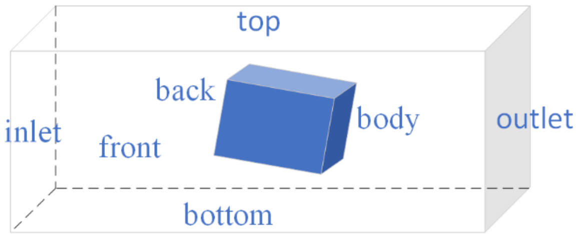

Figure 2. The boundary name of the NWT.

3. Comparison Against Published Data

A 3D numerical wave tank (NWT) is established with the above numerical methods of OpenFOAM and waves2foam. To validate the 3D NWT model, we compare the numerical results of wave interaction with a fixed and vertically suspended cylinder payload with the published data [16].

3.1. Numerical Wave Tank

A 3D numerical wave tank (NWT) is established, as shown in Figure 3. Its geometry has the outer dimensions $15m \times 4m \times 1.2m$ with the water depth $h = 0.505m$ and the relaxation zone of $1.5L$, where L is the wavelength. A cylinder whose radius $a = 0.125m$ is stationary and vertical is suspended in the tank, leaving a $1mm$ gap beneath to the bed of the tank. The length of the cylinder is $1m$. The cylinder is located at $7.5m$ from the paddles in the center of the tank. A wave gauge WG2 is placed $2mm$ in front of the upstream stagnation point of the cylinder to monitor the wave field around the cylinder, and a wave gauge WG1 is placed $0.77m$ from the inlet to monitor the wave elevation.

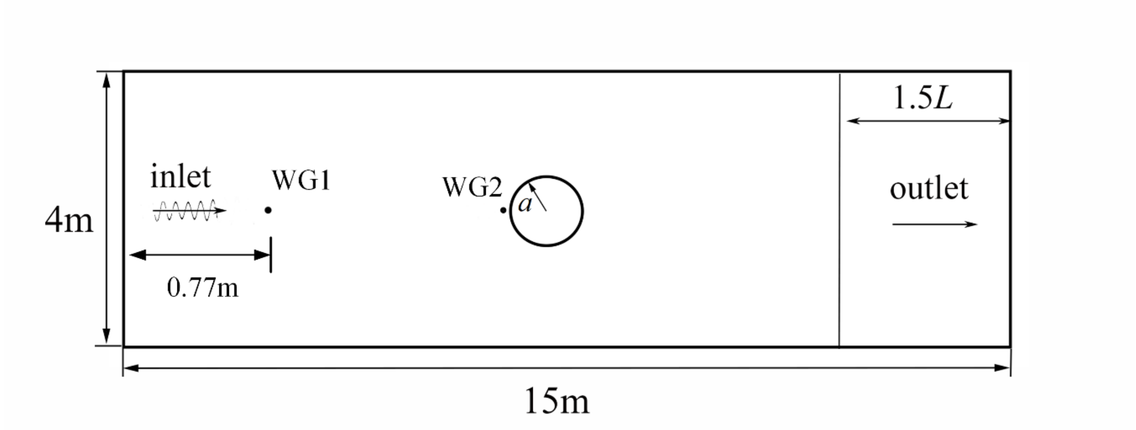

Figure 3. Layout of the numerical wave tank.

Two regular wave cases [16] R1 and R2 are reproduced with our 3D NWT. The wave parameters are shown in Table 1, where h is the water depth, k is the wavenumber, A is the wave amplitude, and T is the wave period.

Table 1. Parameters of regular wave for validation.

Regular Wave	A(m)	T(s)	kh	kA
R1	0.035	1.22	1.39	0.1
R2	0.06	1.63	0.86	0.1

h is the water depth, k is the wavenumber, A is the wave amplitude, and T is the wave period.

The mesh resolution in the computational domain affects the numerical solution. The built-in mesh generator *blockMesh* is used to generate meshes of hexahedral cells, then *snappyHexMesh* in OpenFOAM is used to generate the cylinder. The mesh consists of multilevel grids, as shown in Figure 4. In the areas around the payload, the grid cells have a resolution of Δx in the horizontal direction and Δz in the vertical direction, which are measured by the cells per wavelength and wave height.

Three different time steps are used here for the convergence examination. As shown in Figure 5, three cases are set to a fixed time-step, and the results are convergent. For each time-step, one, two, and three inner iterations (*nOuterCorrectors* in OpenFOAM) are used for convergence examination, the result is the same as Figure 5. For each inner iteration, the PIMPLE algorithm is called three times (*nCorrectors* in OpenFOAM). For the remaining cases in the paper, one *nOuterCorrectors* and three *nCorrectors* are used, the simulation time is 18 s, and the fixed time step is set to 0.005 s, the courant numbers during the simulation are all less than 0.1.

The time history of horizontal force F_x on the cylinder payload with three different mesh schemes for the regular waves are shown in Figure 6. From this grid convergence examination, it can be seen that the results of Mesh 2 and Mesh 3 are convergent and Mesh 2 uses much less time; thus, the intermediate Mesh 2 is selected in this paper. For the Mesh 2 scheme, multilevel grids are used just as Figure 4 shows: in total, 470 cells in the x-direction, 125 cells in the y-direction, and 100 cells in the z-direction. The mesh around the inlet, outlet, and object is dense, and the rest transitions smoothly. The mesh around the cylinder and free surface is uniform: 110 cells per wavelength and 110 cells in total are set in the x-direction, 30 cells per wave height, and 60 cells in total are set in the z-direction and 60 cells in total in 1 m are set in the y-direction.

The simulations are run on purchased Dell T7920 workstation with Intel Xeon (R)E5 2699v4 CPU, 128GB RAM, and 44 cores. The comparison of the computation cost, the total cell numbers, the number of cores, and the simulated time under three different mesh schemes are illustrated in Table 2.

Table 2. Mesh parameters and computation cost.

Mesh Scheme	$\Delta x = \Delta y$	Δz	Cell Number (Million)	Cores	Run Time (h)
1	$L/88$	$H/15$	2.04	24	3.15
2	$L/110$	$H/30$	5.88	24	12.54
3	$L/132$	$H/45$	16.88	24	55.4

L is the wavelength. H is the wave height.

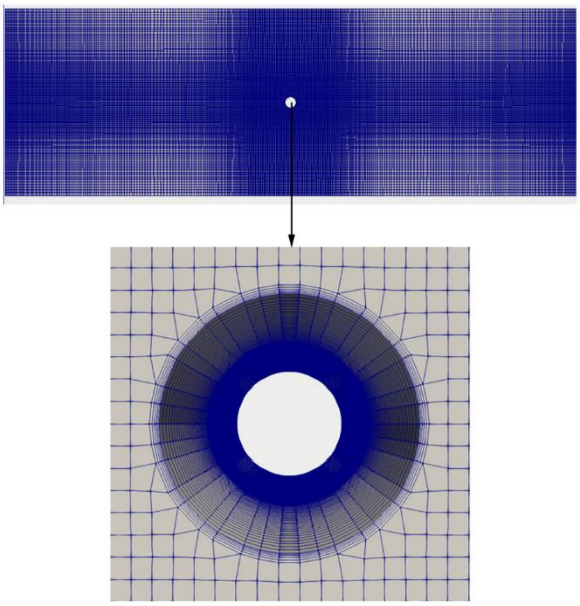

Figure 4. Mesh around the cylinder in the 3D NWT.

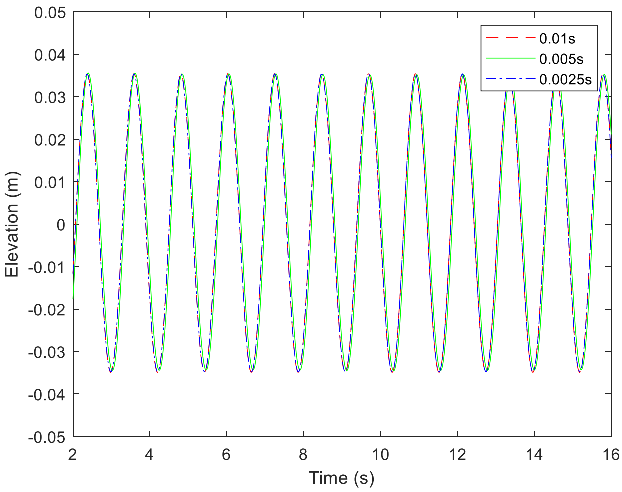

Figure 5. Time history of the surface elevation at WG1 for the wave R1 with three different time-steps.

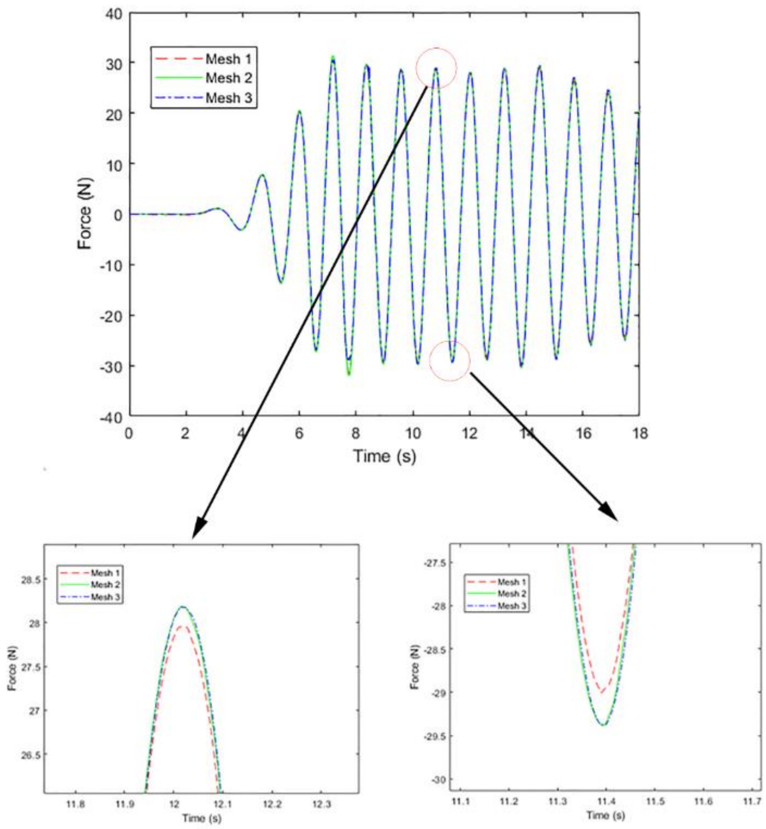

Figure 6. Time history of horizontal force F_x on the cylinder payload with three different mesh schemes for regular wave R1.

3.2. Comparison with the Published Data

Before the simulation, the surface elevation at WG1 for the wave R1 is compared with theory results, the result is as Figure 7 shows, the surface elevation agrees well with the theory. The free surface elevation and horizontal force are compared with published data. The time histories of the free surface elevation at WG2, and the corresponding amplitude spectra obtained by applying the FFT algorithm to the time histories are shown in Figure 8. The surface elevation is normalized by the wave amplitude A, and the time is normalized by the wave period t. The time series of the horizontal force on the cylinder and the corresponding amplitude spectra are presented in Figure 9. The force is normalized by $0.5\rho gAS$, where ρ is density of the water, and S is the cross-sectional area of the payload in the water perpendicular to the wave propagation direction. It can be seen that the results obtained with our NWT model match with the published data [16]. It is validated that our present 3D NWT numerical model can be used to calculate the wave load exerted on the payload with a reasonable degree of accuracy.

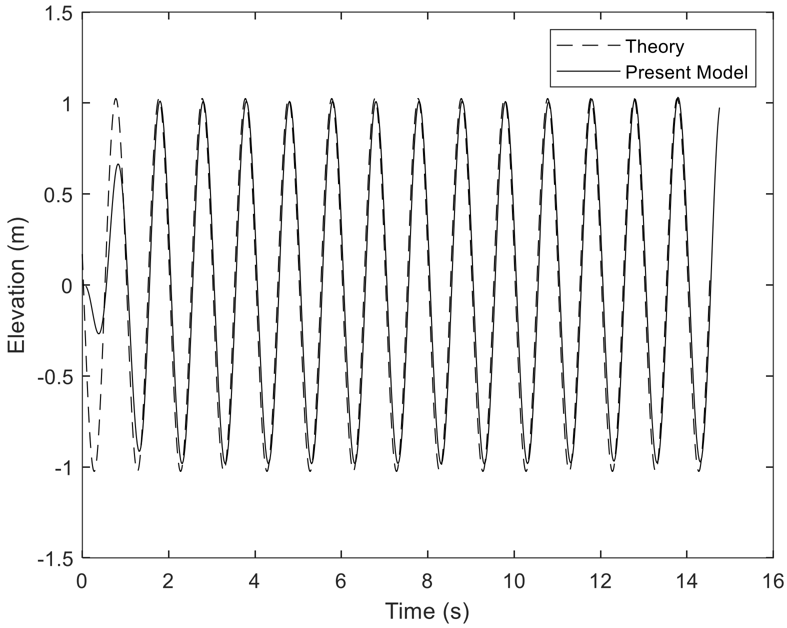

Figure 7. Surface elevation at WG1 for the wave R1 compared with theory result.

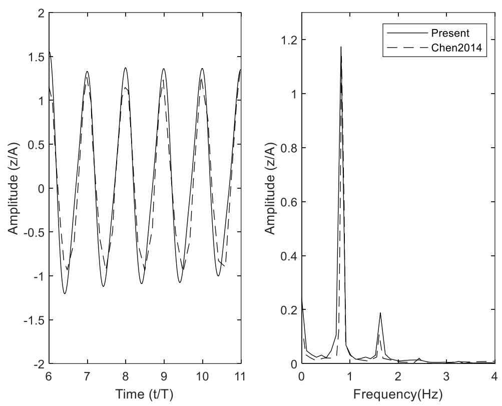

(**a**)

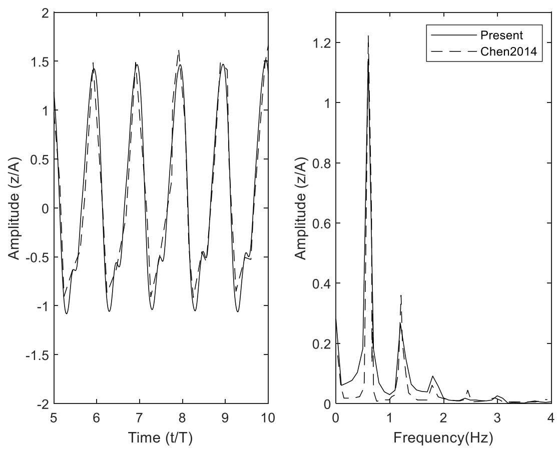

(**b**)

Figure 8. Time series of free surface elevation and amplitude spectra at WG2 for regular wave R1 and R2. (**a**) Results of R1; (**b**) results of R2.

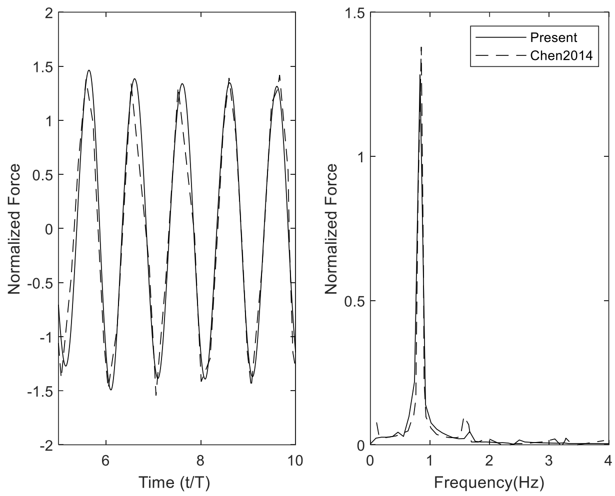

(**a**)

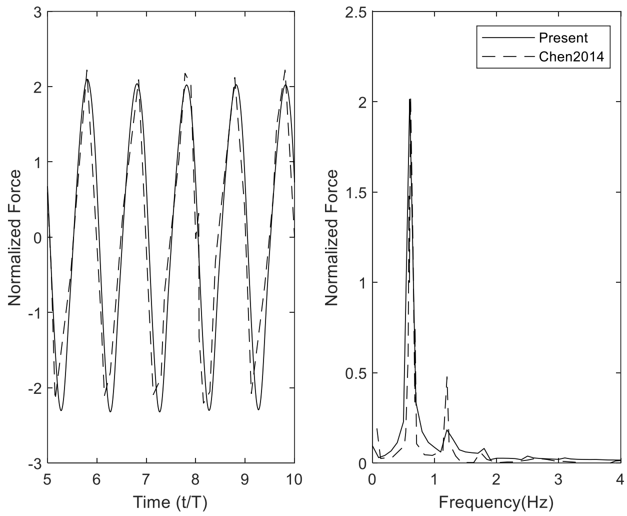

(**b**)

Figure 9. Time series of horizontal force on the cylinder and amplitude spectra for regular wave R1 and R2. (**a**) Results of R1; (**b**) results of R2.

4. Numerical Results

The 3D NWT established in Section 3 is applied in a series of simulation experiments in this section. Our study focuses on the influence of different postures of the payloads on wave forces and moments exerted on the payloads while suspending in the sea. We assume that the payloads are fixed and stationary while suspended in the sea without considering their translational and rotational motions caused by wave forces and rotational moments. A cylinder payload and a cuboid payload with different postures that are fixed and suspended in the regular wave R1 are simulated respectively. F_x, F_y, F_z three forces along the axes $o_b\mathbf{x}_w, o_b\mathbf{y}_w, o_b\mathbf{z}_w$, and M_x, M_y, M_z, three rotational moments about the axes are computed for two payloads. The influence of the postures of the payloads on wave forces and rotational moments exerted on the payloads are analyzed.

4.1. Case 1: A Cylinder Payload Fixed Suspending in the 3D NWT

The same cylinder payload in Section 3 is used here. In this subsection, in addition to the vertical suspension, several postures of the cylinder in the NWT are considered. The posture of the cylinder payload in the 3D NWT is shown in Figure 10. The wave condition is the same as the regular wave R1.

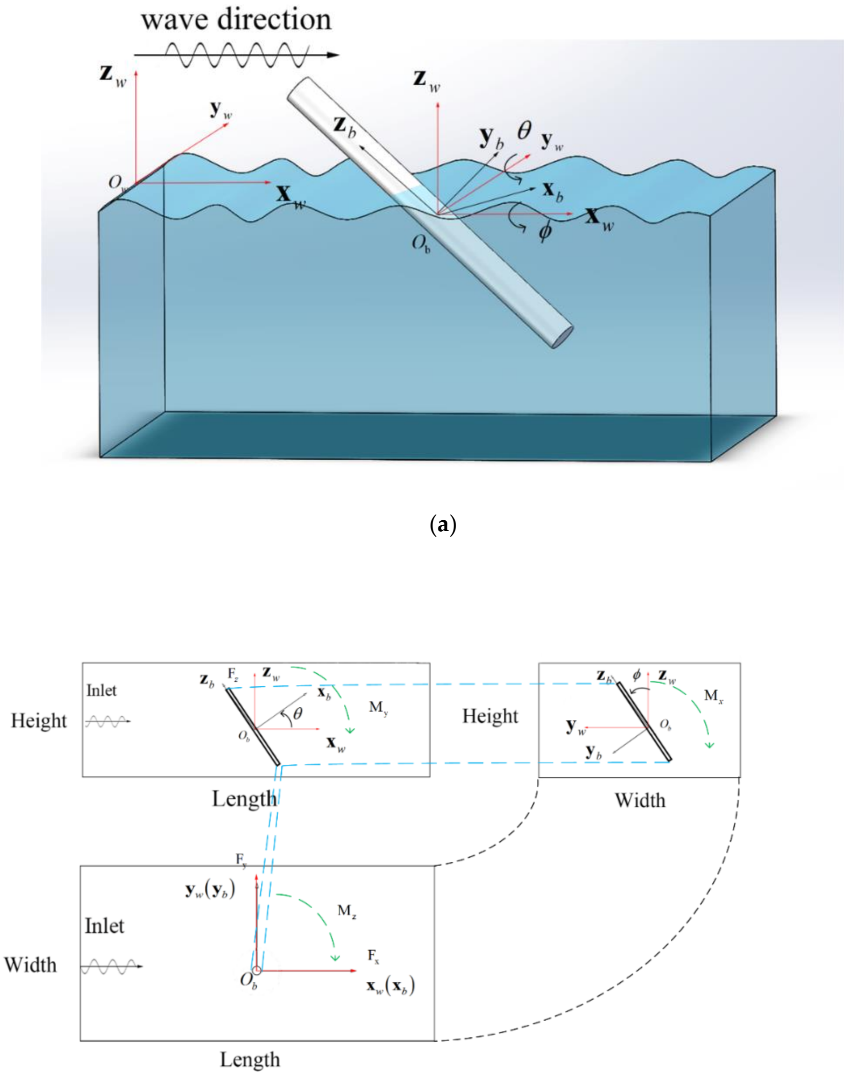

(**a**)

(**b**)

Figure 10. Two different descriptions of frames and the postures of the cylinder payload in the 3D NWT. (**a**) The overall description of two frames and a cylinder payload in the 3D NWT; (**b**) description of Euler angles in the top, side, and front view.

To validate the 3D NWT, the horizontal wave force F_x is compared with results computed by Morison's equation [27]

$$F_x = \rho C_m V\dot{u} + \frac{1}{2}\rho C_d S u\,|\,u\,| \tag{9}$$

where C_m is the added mass coefficient (C_m=1.15), C_d is the drag coefficient (C_d=1), V is the volume of the payload in the water, S is the cross-sectional area of the payload in the water perpendicular to the wave propagation direction, and $\dot{u}$ is the horizontal acceleration.

As shown in Figure 11, the normalized first-harmonic forces and moments are obtained by applying the FFT algorithm to the time histories. The first-harmonic forces are normalized by

$0.5\rho gAS$ and the first-harmonic rotational moments are normalized by $\rho gdAS$ where d is the draft of the cylinder. In the latter study, the same normalization method is used for the forces and moments.

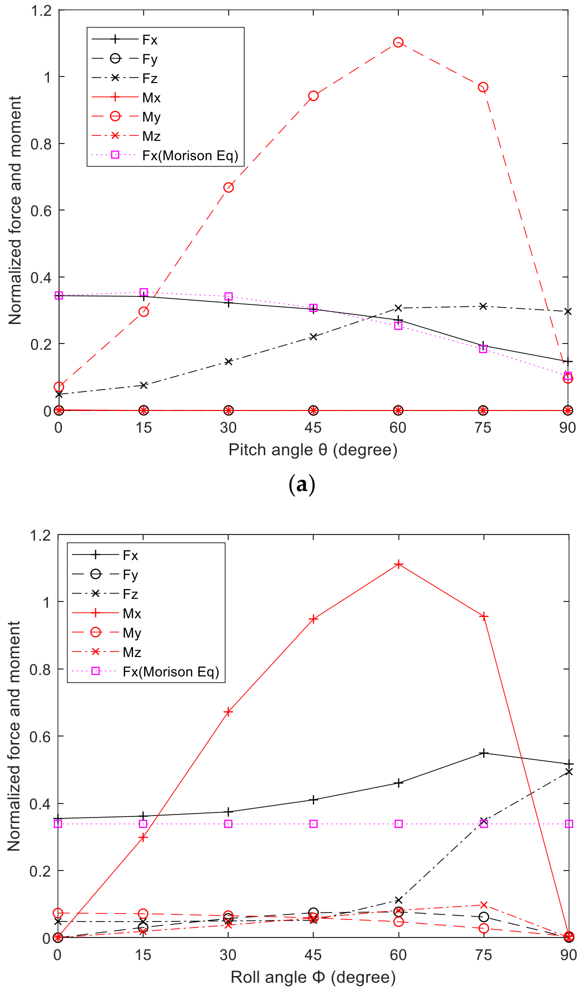

(**a**)

(**b**)

Figure 11. Normalized forces and moments on the cylinder payload versus a single posture angle. **(a)** the pitch angle θ; **(b)** the roll angle ϕ.

1. Pitch angle $\theta = \left(0^0,\ 15^0,\ 30^0,\ 45^0,\ 60^0,\ 75^0,\ 90^0\right)$, roll angle $\phi = 0^0$

In Figure 11a, it can be seen that the horizontal force F_x obtained with the 3D NWT matches with that computed by Morison's equation. The horizontal force F_x decreases with the pitch angle and F_z increases with the pitch angle. This could be explained by the decrease of the projection area of the cylinder on the surface *yoz* and increase of the projection area of the cylinder on the surface xoy.

It is obvious that F_y, the lateral force, and M_y, M_z the rotational moments about x-axis and z-axis, are much less than the others, and can be neglected regardless of pitch angle θ. The numerical results match the physical phenomena and can be explained easily with the force analysis. In the case of $\psi = 0^0, \phi = 0^0$ the rotational moment M_y exerted on the cylinder about y-axis depends on the horizontal force F_x and the vertical force F_z. M_y increases with the increase of θ from 0^0 to 60^0, then it decreases with the increase of θ from 60^0 to 90^0. The maximum moment with $\theta = 60^0$ is 10 times larger than that of vertical suspension.

2. Roll angle $\phi = \left(0^0,\ 15^0,\ 30^0,\ 45^0,\ 60^0,\ 75^0,\ 90^0\right)$, pitch angle $\theta = 0^0$.

In Figure 11b, it can be seen that the horizontal force F_x obtained from the 3D NWT matches with that computed with Morison's equation only for a limited range near to $\phi = 0^0$. The reason is that the two coefficients C_m, C_d change with the increase of the roll angle ϕ . The values of C_m, C_d at $\phi = 0^0$ no longer work with the increase of ϕ .

It can be seen that the lateral force F_y , the rotational moments M_y, M_z , about the y-axis and z-axis are not zero but small values. Both the horizontal force F_x and the vertical force F_z increase with the roll angle ϕ , but F_x decreases when the angle is 75^0 . The projection area of the cylinder on the surface xoy increases with the increase of θ from 0^0 to 90^0 , and the vertical force exerted on the cylinder also increases. The increase is quicker with the roll angel ϕ from 60^0 to 90^0 . The rotational moment M_x increases with the increase of ϕ from 0^0 to 60^0 , and then decreases with the increase of ϕ from 60^0 to 90^0 .

From the above simulations of the two cases, we can see that the changes of force could be explained by the change of the corresponding projection area. Additionally, the moment around a certain axis changes drastically with the change of angle. For example, when the cylinder rotates around the y-axis (pitch angle), the max value of M_y is 10 times larger than the initial value. For the vertical cylinder payload, there is no angle where all the forces and moments are minimal, but the initial posture could be an optimal selection.

4.2. Case 2: A cuboid Payload Fixed Suspending in the 3D NWT

A cuboid payload is fixed and suspended in the 3D NWT as shown in Figure 1. The size of the cuboid is $1m \times 0.5m \times 0.5m$, and the draft is $d = 0.25m$. The cuboid's posture in the 3D NWT is represented by the three Euler angles. A series of simulations are done with different postures of the suspending cuboid in the 3D NWT.

1. Yaw angle $\psi = \left(0^0, 15^0, 30^0, 45^0, 60^0, 75^0, 90^0\right)$, pitch and roll angle $\theta = 0^0$, $\phi = 0^0$.

The normalized forces and moments on the cuboid payload versus its yaw angle ψ are shown in Figure 12a. With the normal incident regular waves, the horizontal force F_x decreases with the increase of ψ from 0^0 to 90^0 . The projection area on the surface yoz is the biggest when $\psi = 0^0$. The projection area on the surface yoz decreases with the increase of ψ from 0^0 to 90^0 . It can be seen only F_x changes drastically with the angle, which is not the same as the results of cylinder where the moment changes drastically.

2. Pitch angle $\theta = \left(0^0, 15^0, 30^0, 45^0, 60^0, 75^0, 90^0\right)$, yaw and roll angle $\psi = 0^0$, $\phi = 0^0$.

The normalized forces and moments on the payload versus the pitch angle θ are shown in Figure 12b. It is obvious that both the lateral force F_y and the rotational moment M_x and M_z are near to zero no matter the pitch angle. The horizontal force F_x , the vertical force F_z .and the rotational moment M_y are all symmetrical around 45^0 . This could be easily explained by the change in the projection area. When the pitch angle θ increases from 0^0 to 45^0 , the horizontal force F_x decreases. Additionally, it increases when θ increases from 45^0 to 90^0 . At $\theta = 0^0, 90^0$, the regular waves which are normally incident to the cuboid's face with the largest surface area exert the maximum horizontal force on the cuboid. It can be seen that there is also not a drastically changed moment with the change of the angle.

3. Roll angle $\phi = \left(0^0, 15^0, 30^0, 45^0, 60^0, 75^0, 90^0\right)$, pitch, yaw angle $\theta = 0^0$, $\psi = 0^0$.

The normalized forces and moments on the cuboid payload versus the roll angle ϕ are shown in Figure 12c. It can be seen that compared with M_x , the changes of other forces and moments are small, and M_x increases very quickly with the increase of ϕ from 0^0 to 30^0 , and decreases with ϕ from 30^0 to 90^0 . The phenomenon of a drastically changed moment is similar to the results of the cylinder.

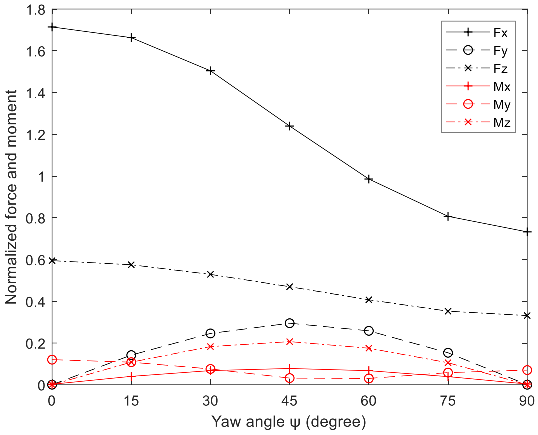

(**a**)

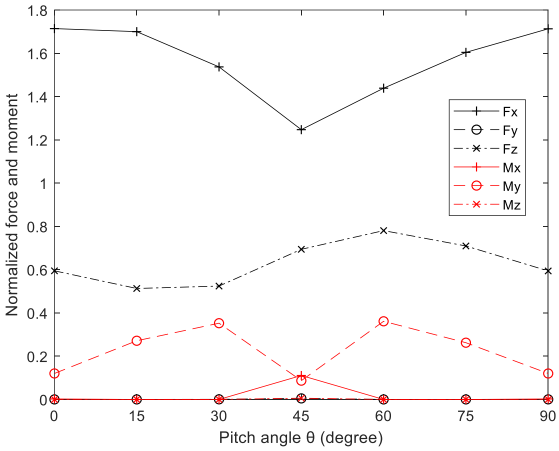

(**b**)

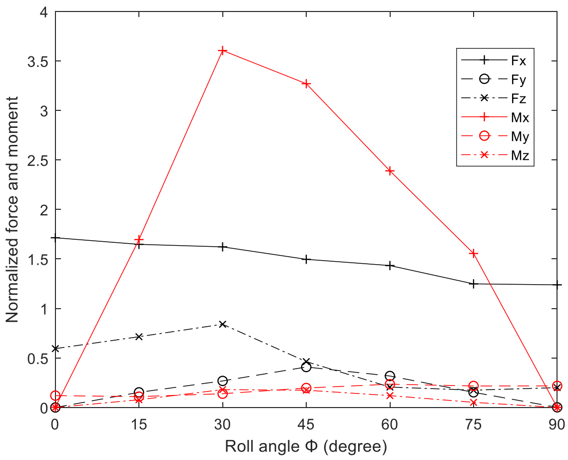

(**c**)

Figure 12. Normalized forces and moments on the cuboid payload versus a single posture angle. (**a**) the yaw angle ψ ; (**b**) the pitch angle θ ; (**c**) the roll angle ϕ .

For the two cases of the cylinder, the moment changes drastically with the angle. For the three cases of the cuboid payload, when the cuboid payload rotates around the x-axis (roll angle), the change of force and moment is similar to the cylinder cases. The changes of force could be explained by the change of the corresponding projection area, and the moment around a certain axis changes drastically with the change of angle. However, results when rotating around the z-axis (yaw angle) and y-axis (pitch angle) show no drastically changed moment.

To show that the difference could be brought by the initial posture, we plot the normalized forces and moments on the cylinder payload versus its yaw angle ψ when the roll angle $\phi=90^0$, just as Figure 13 shows. It can be seen that the result is similar to Figure 12a,b. When the roll angle $\phi=90^0$, the cylinder is horizontally placed, its length side along the y-axis. When this happens, the phenomenon of a drastically changed moment disappears.

For further study, we also plot the result when the vertically placed cuboid payload rotates around the y-axis and z-axis. Just as Figure 14 shows, the result is similar to Figure 12c. When the cuboid is vertically placed and the roll angle $\phi=90^0$, its long side along the z-axis. However, in Figure 14b, there is an exception, the drastically changed moment is not around the z-axis but the y-axis, other results are all as expected.

All three above figures show that the drastically changed moment is brought about by the initial posture. The moment around a certain axis changes drastically with the change of angle when the payload is vertically placed (which means the long side of the payload is vertical to the water surface) such as in Figure 14, and this phenomenon could happen when the horizontally placed payload changes to the vertical posture, such as in Figure 12c.

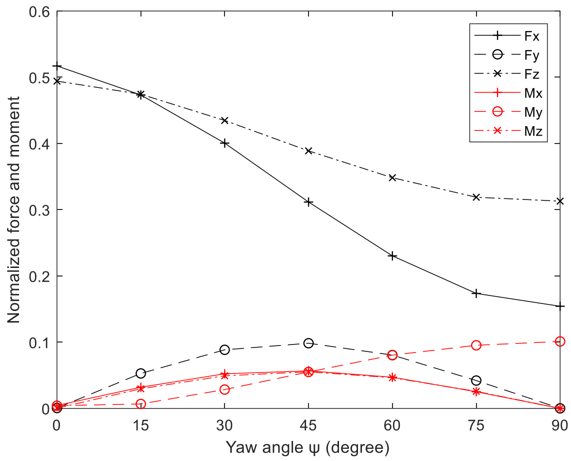

Figure 13. Normalized forces and moments on the cylinder payload versus its yaw angle ψ when the roll angle $\phi=90^0$

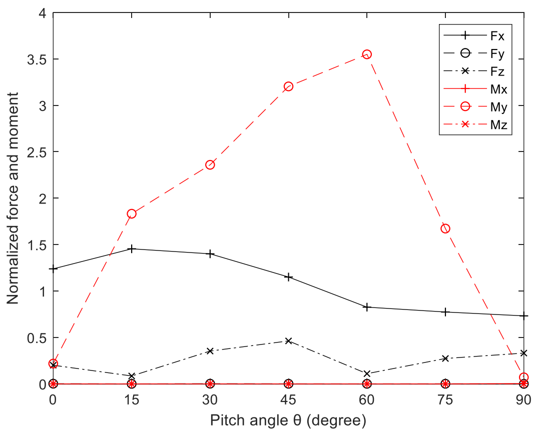

(**a**)

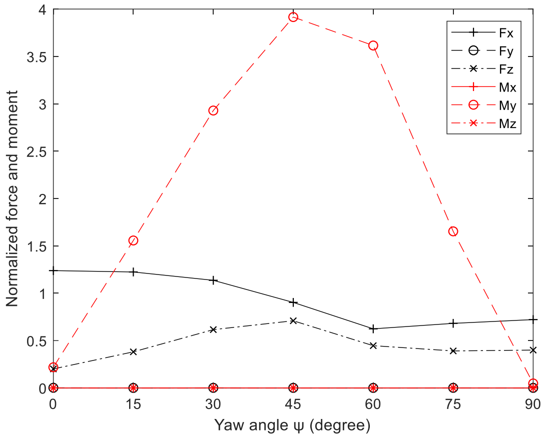

(**b**)

Figure 14. Normalized forces and moments on the cuboid payload versus a single posture angle when the roll angle ϕ=90^0. (**a**) the pitch angle θ; (**b**) the yaw angle ψ.

4. Yaw ψ and roll ϕ concurrently change from 0^0 to 90^0, pitch $\theta = 0^0$.

The force and moment exerted on the cuboid versus the yaw angle ψ and the roll angle ϕ is shown in Figures 15 and 16. For the horizontal force F_x, it decreases with the yaw angle ψ regardless of the roll angle ϕ. When the roll angle is 0^0, the cuboid is horizontally placed, with its long side vertical to the wave direction when the yaw angle is 0^0. When the roll angle increases from 0^0 to 90^0, the long side gradually changes to the vertically placed position; thus, the gradient along the yaw angle decreases with the increase of the roll angle. For the lateral force F_y, the result is symmetrical about yaw angle and roll angle.

The results of M_x could also be explained by the conclusion raised above. When the yaw angle is 0^0, the roll angle increases to 90^0, the cuboid changes from horizontally placed to be vertically placed, and the M_x changes drastically with the roll angle. When the yaw angle is 90^0, the cuboid payload could not change to be vertically placed with the change of roll angle, and the phenomenon of a drastically changed moment disappears. When the yaw angle change from 0^0 to 90^0, the phenomenon gradually disappears.

The result of M_y and M_z demonstrate the exceptional condition in Figure 14b. When the roll angle is 0^0, the cuboid is horizontally placed, and there is no drastically changed moment. When the roll angle is 90^0, the cuboid is vertically placed and the moment M_y, instead of M_z, drastically changes with the yaw angle. There is also a transition when the roll angle increases from 0^0 to 90^0. The amplitude of M_z is much less than the others, and can be neglected.

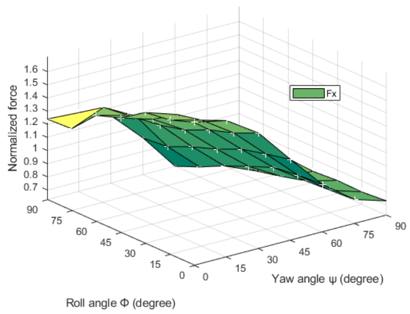

(**a**)

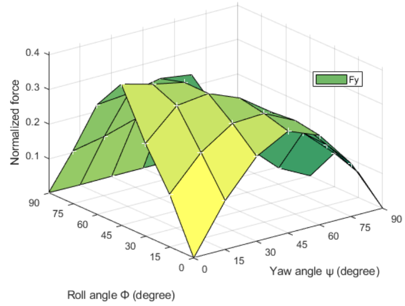

(**b**)

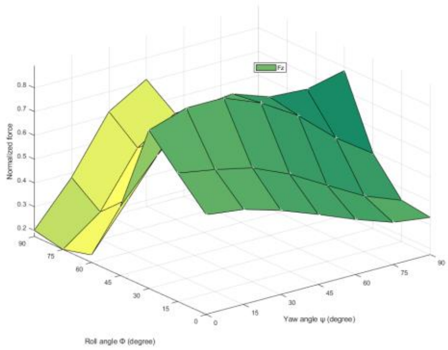

(**c**)

Figure 15. Normalized force on the cuboid payload versus yaw ψ and roll ϕ. (**a**) the horizontal force F_x; (**b**) the lateral force F_y; (**c**) vertical force F_z.

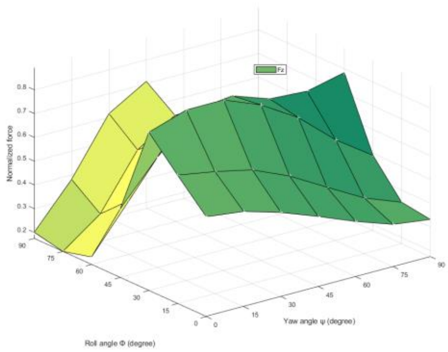

(**a**)

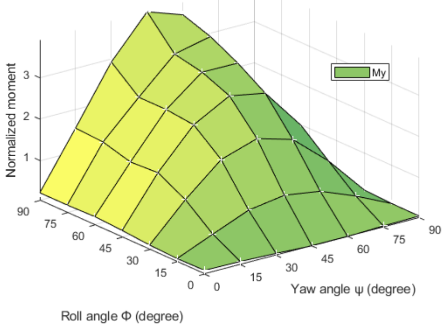

(**b**)

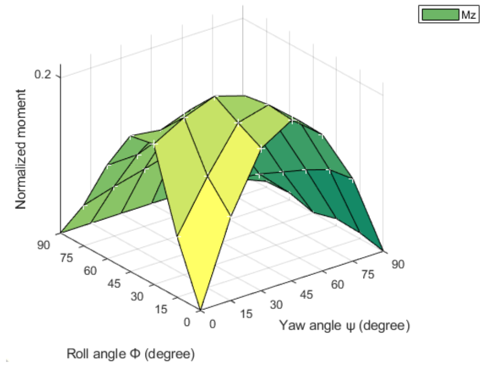

(**c**)

368 **Figure 16.** Normalized moment on the cuboid payload versus yaw ψ and roll ϕ. (**a**) the horizontal
369 moment M_x; (**b**) the lateral moment M_y; (**c**) vertical moment M_z.

370 *4.3. Parameter Studies*

371 The parameter studies are done to analyze the effects of the cuboid's size and wave parameters
372 on the forces and moments exerted on the cuboid payload. Here, in order to focus on the effects of
373 cuboid's size and wave parameters, no posture angles are considered and the cuboid is horizontally
374 placed.

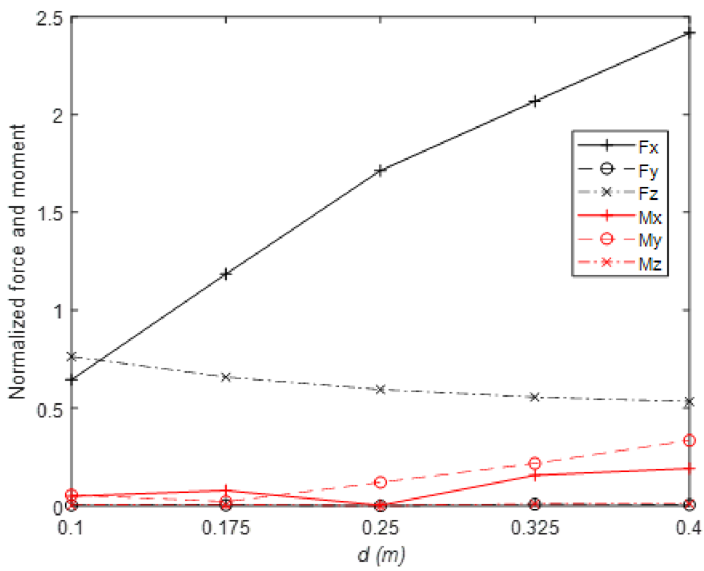

(**a**)

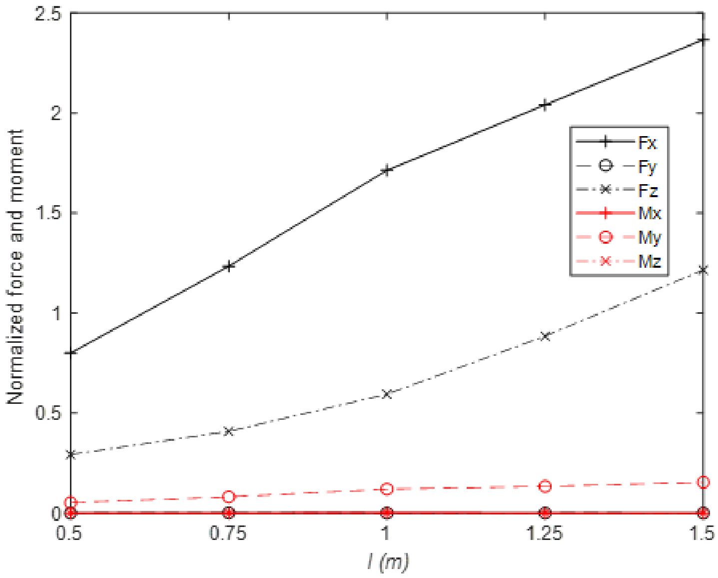

(**b**)

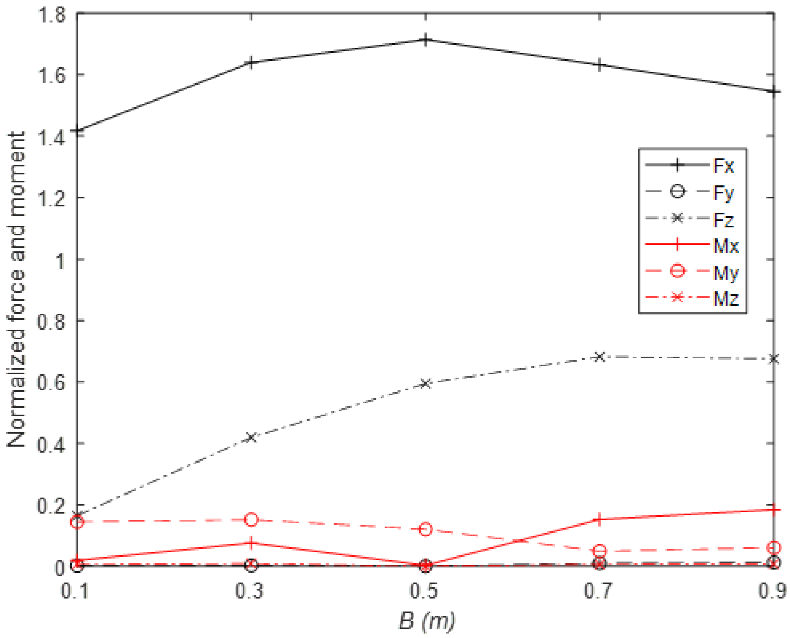

(**c**)

Figure 17. Normalized forces and moments on the cuboid payload with different size parameters. (**a**) with different drafts; (**b**) with different lengths; (**c**) with different widths.

1. Cuboid's size effects on forces and moments

The normalized forces and moments on the cuboid payload with different drafts, lengths, and widths are shown in Figure 17 a–c. The results show that the horizontal force F_x increases with the increase of the payload draft and length. The vertical force F_z decreases slowly with the increase of the draft and increases with the length and width. The rotational moment M_y increases slowly with the increase of the payload draft d. The change of other forces and moments can be neglected.

2. Wave's parameters effects on forces and moments

The normalized forces and moments on the cuboid payload with different drafts, lengths, and widths are shown in Figure 18a,b. It can be seen that both the horizontal force F_x and the vertical force F_z increase with the increase of the wave amplitude and wavelength. The change of other forces and moments could be neglected.

From the above parameter simulations, we can see that the horizontal force F_x and the rotational moment M_y exerted on the cuboid payload increase with the increase of its draft d, and its length l. The vertical force F_z and the rotational moment M_x increase with its width B. The increase of the wave amplitude A and wave length L cause the increase of the horizontal force F_x and the vertical force F_z.

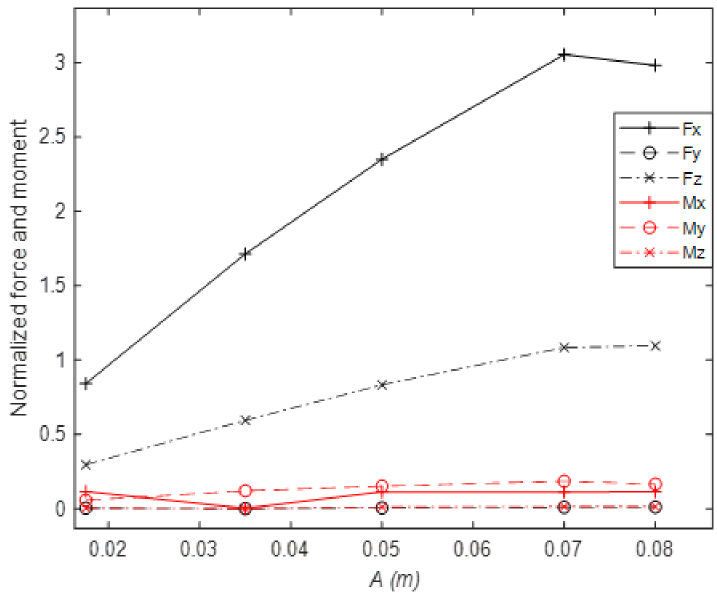

(**a**)

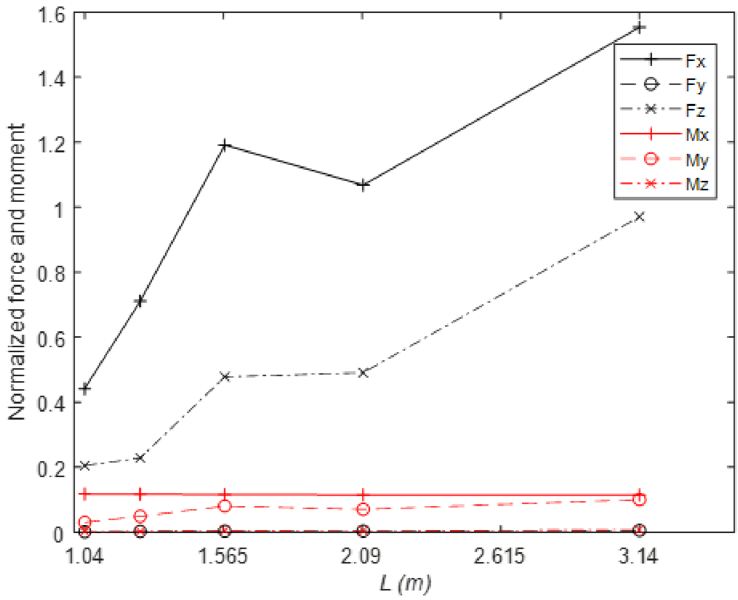

(**b**)

Figure 18. Normalized forces and moments on the cuboid payload with different wave parameters. (**a**) different wave amplitudes; (**b**) different wavelengths.

5. Conclusions

In order to investigate regular wave interaction with a fixed suspending payload with different postures, a three-dimension NWT based on OpenFOAM and waves2foam is established. Regular wave interaction with a vertically suspended cylinder is investigated. The free surface elevation, horizontal wave force, as well as the corresponding amplitude spectra obtained by the FFT algorithm, are compared with the theory result and the results reported in [16] for validation. Then, the representation of the payload's posture in the regular wave is given. The forces and moments exerted on a suspended cylinder and a suspended cuboid with different postures are investigated separately. Finally, parameter studies in the case of payload's size wave parameters are considered.

It can be concluded that the moment around a certain axis changes drastically with the change of the same angle when the payload is initially vertically placed (which means the long side of the payload is vertical to the water surface). For example, the moment around the y-axis could change drastically when rotating around the y-axis. This phenomenon could also happen when the horizontally placed payload (which means the long side parallel to the sea level) changes to the vertical posture. There is an exception: when rotated around the z-axis, the drastically changed moment is not around the z-axis but the y-axis. Therefore, for the rectangular shape payload, it is better to keep the payload horizontally placed to prevent the drastic change of the moment. Additionally, the projection area of the payload vertical to the direction of force affects the corresponding force. It is better to keep the short side vertical to the incident direction of the wave; thus, a minimal horizontal force can be obtained. Through the simulations, some certain posture of the payload with the minimum forces and moments can be reached. It can guide the design of control strategies for the safe operation of offshore cranes, such as keeping the payload to a certain posture that suffers minimal force and moment or changing the controller weight of some forces and moments under specific circumstances.

Author Contributions: Conceptualization, Mingwei Yan and Xin Ma; data curation, Mingwei Yan; formal analysis, Mingwei Yan and Xin Ma; funding acquisition, Xin Ma; investigation, Mingwei Yan; methodology, Mingwei Yan; project administration, Xin Ma and Yibin Li; resources, Mingwei Yan; Software, Mingwei Yan, Wei Bai and Zaibin Lin; supervision, Xin Ma; validation, Mingwei Yan; Visualization, Mingwei Yan; writing—original draft preparation, Mingwei Yan; writing—review and editing, Mingwei Yan, Xin Ma and Wei Bai.

Funding: This research was funded by the Joint Fund of the National Nature Science Foundation of China and Shandong Province, grant number No. U1706228.

Conflicts of Interest: The authors declare no conflicts of interest.

References

1. DNV. *Modelling and analysis of marine operations*; DNV Offshore Standards: Hovik, Norway, 2011.
2. Chau, F.; Taylor, R.E. Second-order wave diffraction by a vertical cylinder. *J. of Fluid Mech.* **1992**, *240*, 571–599.
3. Hunt, J.; Baddour, R. The diffraction of nonlinear progressive waves by a vertical cylinder. *Q. J. Mech. Appl. Math.* **1981**, *34*, 69–87.
4. Bai, W.; Taylor, R.E. Numerical simulation of fully nonlinear regular and focused wave diffraction around a vertical cylinder using domain decomposition. *Appl. Ocean Res.* **2007**, *29*, 55–71.
5. del Jesus, M.; Lara, J.L.; Losada, I.J. Three-dimensional interaction of waves and porous coastal structures: Part I: Numerical model formulation. *Coast. Eng.* **2012**, *64*, 57–72.
6. Lara, J.L.; del Jesus, M.; Losada, I.J. Three-dimensional interaction of waves and porous coastal structures: Part II: Experimental validation. *Coast. Eng.* **2012**, *64*, 26–46.
7. Lin, P. A multiple-layer σ-coordinate model for simulation of wave–structure interaction. *Comput. Fluids* **2006**, *35*, 147–167.
8. Kang, A.; Lin, P.; Lee, Y.J.; Zhu, B. Numerical simulation of wave interaction with vertical circular cylinders of different submergences using immersed boundary method. *Comput. Fluids* **2015**, *106*, 41–53.
9. Ren, B.; Wen, H.; Dong, P.; Wang, Y. Numerical simulation of wave interaction with porous structures using an improved smoothed particle hydrodynamic method. *Coast. Eng.* **2014**, *88*, 88–100.
10. Didier, E.; Martins, R.; Neves, M.G. Numerical and Experimental Modeling of Regular Wave Interacting with Composite Breakwater. *Int Soc. Offshore Polar Eng.* **2013**, *23*, 9.

11. Ji, Q.; Dong, S.; Luo, X.; Soares, C.G. Wave transformation over submerged breakwaters by the constrained interpolation profile method. *Ocean Eng.* **2017**, *136*, 294–303.
12. Wang, J.-H.; Zhao, W.-W.; Wan, D.-C Development of naoe-FOAM-SJTU solver based on OpenFOAM for marine hydrodynamics. *J. Hydrodyn.* **2019**, *31*, 1–20.
13. Liu, Z.H.; Wan, D.C.; Hu, C.H. Numerical investigation of regular waves interaction with two fixed cylinders in tandem arrangement. In Proceedings of 37th ASME International Conference on Ocean, Offshore and Arctic Engineering, Madrid, Spain, 2018, ASME: New York, NY, USA 2018.
14. Lara, J.; Higuera, P.; Maza, M.; del Jesus, M.; Losada, I.J.; Barajas, G. Forces induced on a vertical breakwater by incident oblique waves. In Proceedings 33rd Conference on Coastal Engineering, Santander, Spain, Santander, Spain, 1–6 July 2012; Coastal Engineering Proceedings: Santander, Spain, 2012.
15. Higuera, P.; Lara, J.L.; Losada, I.J. Three-dimensional interaction of waves and porous coastal structures using OpenFOAM®. Part I: Formulation and validation. *Coastal Eng.* **2014**, *83*, 243–258.
16. Chen, L.; Zang, J.; Hillis, A.; Morgan, G.; Plummer, A. Numerical investigation of wave–structure interaction using OpenFOAM. *Ocean Eng.* **2014**, *88*, 91–109.
17. Teng, B.; Zhang, X.; Ning, D. Interaction of oblique waves with infinite number of perforated caissons. *Ocean Eng.* **2004**, *31*, 615–632.
18. Fang, Q.H.; Hong, R.C.; Guo, A.X.; Stansby, P.K.; Li, H. Analysis of hydrodynamic forces acting on submerged decks of coastal bridges under oblique wave action based on potential flow theory. *Ocean Eng.* **2018**, *169*, 242–252.
19. Zheng, Y.-H.; Shen, Y.-M.; Ng, C.-O. Effective boundary element method for the interaction of oblique waves with long prismatic structures in water of finite depth. *Ocean Eng.* **2008**, *35*, 494–502.
20. Abul-Azm, A.; Gesraha, M. Approximation to the hydrodynamics of floating pontoons under oblique waves. *Ocean Eng.* **2000**, *27*, 365–384.
21. Gesraha, M.R. Analysis of Π shaped floating breakwater in oblique waves: I. Impervious rigid wave boards. *Appl. Ocean Res.* **2006**, *28*, 327–338.
22. Zheng, Y.; Liu, P.; Shen, Y.; Wu, B.; Sheng, S. On the radiation and diffraction of linear water waves by an infinitely long rectangular structure submerged in oblique seas. *Ocean Eng.* **2007**, *34*, 436–450.
23. Zheng, Y.; Shen, Y.; You, Y.; Wu, B.; Jie, D. Wave radiation by a floating rectangular structure in oblique seas. *Ocean Eng.* **2006**, *33*, 59–81.
24. Song, H.; Tao, L. Wave Interaction with an Infinite Long Horizontal Elliptical Cylinder. In Proceedings of 30th International Conference on Ocean, Offshore and Arctic Engineering, Rotterdam,The Netherlands, 19–24 June 2011; ASME: New York, N.Y, USA, 2011; pp. 589–597.
25. Weller, H.G.; Tabor, G.; Jasak, H.; Fureby, C. A tensorial approach to computational continuum mechanics using object-oriented techniques. *Comput. Phys.* **1998**, *12*, 620–631.
26. Jacobsen, N.G.; Fuhrman, D.R.; Fredsøe, J. A wave generation toolbox for the open-source CFD library: OpenFoam®. *Int. J. Numer. Methods Fluids* **2012**, *70*, 1073–1088.
27. Morison, J.; Johnson, J.; Schaaf, S. The force exerted by surface waves on piles. *J. Pet. Technol.* **1950**, *2*, 149–154.